

# Electrical Conductivity Imaging via Contactless Measurements

Nevzat G. Gençer,\* *Member, IEEE*, and M. Nejat Tek, *Student Member, IEEE*

**Abstract**—A new imaging modality is introduced to image electrical conductivity of biological tissues via contactless measurements. This modality uses magnetic excitation to induce currents inside the body and measures the magnetic fields of the induced currents. In this study, the mathematical basis of the methodology is analyzed and numerical models are developed to simulate the imaging system. The induced currents are expressed using the  $\vec{A}$ - $\phi$  formulation of the electric field where  $\vec{A}$  is the magnetic vector potential and  $\phi$  is the scalar potential function. It is assumed that  $\vec{A}$  describes the primary magnetic vector potential that exists in the absence of the body. This assumption considerably simplifies the solution of the secondary magnetic fields caused by induced currents. In order to solve  $\phi$  for objects of arbitrary conductivity distribution a three-dimensional (3-D) finite-element method (FEM) formulation is employed. A specific  $7 \times 7$ -coil system is assumed nearby the upper surface of a  $10 \times 10 \times 5$ -cm conductive body. A sensitivity matrix, which relates the perturbation in measurements to the conductivity perturbations, is calculated. Singular-value decomposition of the sensitivity matrix shows various characteristics of the imaging system. Images are reconstructed using 500 voxels in the image domain, with truncated pseudoinverse. The noise level is assumed to produce a representative signal-to-noise ratio (SNR) of 80 dB. It is observed that it is possible to identify voxel perturbations (of volume  $1 \text{ cm}^3$ ) at 2 cm depth. However, resolution gradually decreases for deeper conductivity perturbations.

**Index Terms**—Electrical conductivity, finite-element method (FEM), magnetic induction, medical imaging.

## I. INTRODUCTION

**I**MAGING the electrical conductivity of living tissues has been a fundamental challenge in biomedicine. There are a number of techniques that were proposed to obtain the electrical conductivity distribution of the human body [1], [2]. All these techniques use electrodes attached on the body surface to inject current and/or measure voltages. In this study, a new medical imaging modality that makes use of contactless measurements is introduced to image the conductivity distribution. The ultimate goal of this technique is to image the spatio-temporal conductivity changes by magnetic coupling. This provides images of static and time varying conductivities of living tissues.

Manuscript received July 29, 1998; revised March 22, 1999. This work was supported in part by the Middle East Technical University Research Fund under Project AFP-96-03-01-01. The Associate Editor responsible for coordinating the review of this paper and recommending its publication was J. Newell. Asterisk indicates corresponding author.

\*N. G. Gençer and M. N. Tek are with the Electrical and Electronics Engineering Department, Middle East Technical University, 06531 Balgat, Ankara, Turkey (e-mail: ngencer@ed.eee.metu.edu.tr).

Publisher Item Identifier S 0278-0062(99)07428-5.

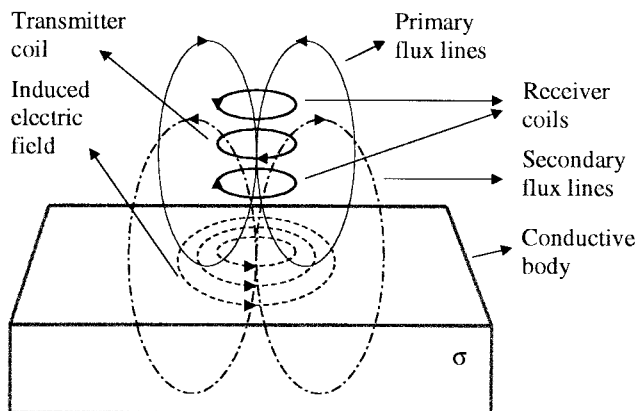


Fig. 1. General principles of data collection in the magnetic-induction magnetic-measurement system. A transmitter coil is energized with low-frequency sinusoidal currents, generating time-varying magnetic fields. This induces current in the nearby conductive body. A receiver coil senses the magnetic fields of both primary current in the transmitter coil, and the induced current in the conductive body.

Fig. 1 shows the basic principles of the measurement system (magnetic-induction magnetic-measurement system). A transmitter coil is driven by a low-frequency sinusoidal current to provide time-varying magnetic fields. When a conductive body is brought near these coils, induced currents in the body are proportional to the conductivity distribution. These currents create secondary magnetic fields and the electromotive force (emf) induced in a receiver coil is measured. This measurement methodology has been known for decades. It was a major technological advance in the field of geophysical inspection [3], [4] (see [3] for an historical perspective). However, it has also been used for different purposes, such as measuring the degree of salt content in sea water or measuring the impurity ratio in semiconductors [3]. For medical purposes, it was first used thirty years ago. In 1968, Tarjan and McFee introduced a magnetically coupled instrument to determine the effective electrical resistivity of the human torso and head [5], [6]. They also observed conductivity fluctuations as a result of cardiac activity and ventilation. These encouraging results show the possibility of a new medical imaging modality, based on this measurement technique.

In conventional applied-current electrical impedance tomography (ACEIT), low-frequency sinusoidal currents are applied via electrodes attached to the body surface [1], [7]–[10]. This technique has been used in characterization of cancerous tissues [18], [19], respiratory medicine [20], [21], localization of cardiac-related impedance changes in the thorax

[22], gastric-function assessment [23], monitoring conductivity changes in the adult brain during the cardiac cycle [24], [25], in thermal monitoring of hyperthermia treatment [26], and in the localization of epileptic foci [28], [29]. However, the use of current injection from the surface electrodes has some limitations that affect the performance of the imaging system [11], [15]. In addition, an insulating layer (such as bone) near the injection electrodes reduces the injected current density in the deep-lying tissues. This is an important problem, especially when the head is to be imaged. Note that the electrical-conductivity distribution of the human head is also necessary to develop realistic electrical models, required to increase the accuracy in locating electrical sources in the human brain [30]–[32].

In induced-current electrical impedance tomography (ICEIT), currents are induced into the body by time-varying magnetic fields (e.g., 50 kHz) [11]–[15]. Thus, it is possible to eliminate the screening effect of bones. In addition, by applying different magnetic fields it is possible to increase the number of measurements. This can be achieved by using different coil shapes, or by changing the position of a given coil. In ACEIT, the number of measurements can be increased by increasing the number of electrodes attached on the body surface. In that sense, ICEIT is more flexible as compared to ACEIT. However, a common problem of both techniques is the attachment of electrodes to the body surface to measure the voltages.

Compared to the above techniques, the proposed technique has the following important features: 1) there is no physical contact between the body and the measurement system; 2) currents can be coupled into the body avoiding screening effect of the superficial insulating layers; and 3) the number of measurements can be increased by simply shifting the transmitter and receiver coil array. In addition, the proposed technique can be used to obtain both static (actual) and dynamic (difference) images.

The feasibility of the proposed measurement system for medical imaging purposes was explored in [33]. The validity of the simplifying assumptions for the governing field equations were investigated. It was found that for an operating frequency of 100 kHz, the displacement currents can be ignored. However, the propagation effects become significant for a representative distance of 20 cm. In order to estimate the induced current densities and their magnetic fields (secondary fields), the half-space problem was solved for coplanar and coaxial coil configurations (Fig. 2), where analytical solutions are available (see the Appendix for detailed formulation). For a coaxial coil configuration, the maximum induced current density was on the order of  $10^{-5}$  mA/cm<sup>2</sup>, whereas the secondary voltage was about 10  $\mu$ V. These results were obtained for a one-turn transmitter coil of radius 1 cm, excited by a sinusoidal current of 1 A peak at 50 kHz. The detection coil was assumed to be of the same size, but with 10 000 turns. For a coplanar coil configuration, the maximum current density increased to  $4.9 \times 10^{-4}$  mA/cm<sup>2</sup> and the secondary voltage was about 10  $\mu$ V. Note that the calculated maximum current densities are much lower than the safety limit (1.6 mA/cm<sup>2</sup> at 50 kHz [34]), whereas the received voltages are measurable.

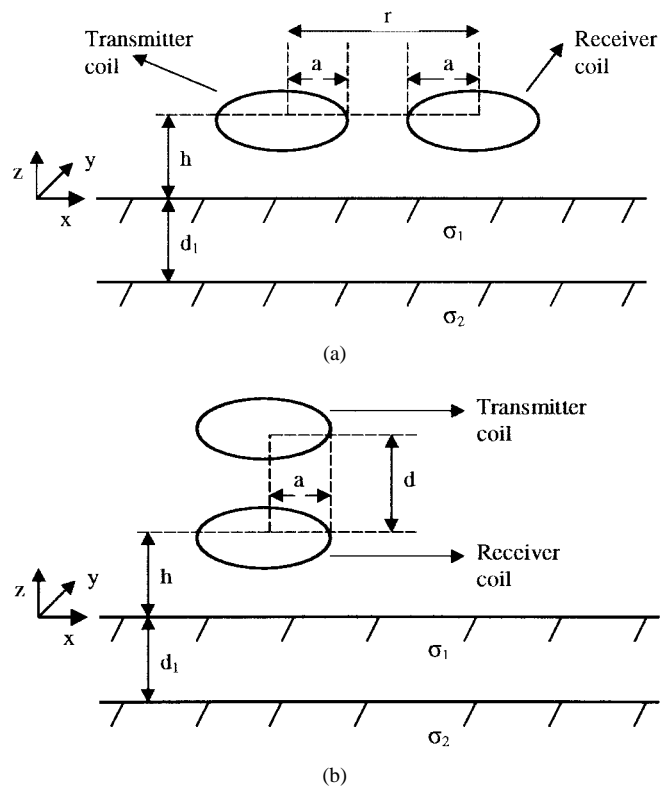


Fig. 2. Possible coil configurations for magnetic-induction magnetic measurement system. (a) Coplanar configuration. (b) Coaxial coil configuration.

The above results were obtained using analytical expressions, assuming that the conductive body is a half space. However, in general, the solution for current densities and the secondary magnetic fields must be obtained numerically for bodies of arbitrary geometries and conductivity distributions. In this study, the finite-element method (FEM) is employed to solve the scalar potential functions and, therefore, the induced currents in the conductive medium. The performance of the numerical model was tested with analytical solutions and with the results reported for standard problems [17]. In that study, the numerical model has also been used to explore the changes in the potential and secondary magnetic field patterns, caused by conductivity perturbations in a cubic conductive body. Currents were induced in a  $9 \times 9 \times 5$  body of conductivity  $0.2 \text{ Sm}^{-1}$ , by circular coils driven sinusoidally (10 kHz). It was found that a 1-cm shift in the perturbation depth reduces the field magnitude to approximately one-tenth. In addition, the distance between the field extrema increases with the perturbation depth.

In the first part of this study, the forward problem (i.e., calculation of measurements for a given conductivity distribution) formulation is presented. An expression is derived, relating the first-order variation in the secondary magnetic fields to the conductivity perturbations in the conductive body. The FEM is used to numerically implement this relation. The sensitivity matrix, which relates the perturbation in measurements to the conductivity perturbations, is calculated. In the second part, the characteristics of the inverse problem (i.e., calculation of the conductivity distribution using the measurements) are explored

by analyzing the properties of the sensitivity matrix. Images reconstructed with simulated data are also presented.

## II. FORMULATION OF THE FORWARD PROBLEM

### A. Relation of Magnetic Flux Density to Induced Currents

For sinusoidally varying electromagnetic fields ( $e^{j\omega t}$  time dependence is assumed) in a linear isotropic nonmagnetic conductive medium, the electric field  $\vec{E}$  can be expressed as follows:

$$\vec{E} = -j\omega\vec{A} - \nabla\phi \quad (1)$$

where  $\omega$  is the radial frequency,  $\vec{A}$  is the magnetic vector potential, and  $\phi$  is the scalar potential [35].

Equation (1) shows that the electric field has two sources: variation of magnetic field with time and surface and volume charges. Finding  $\vec{E}$  is considerably simplified under the following assumptions: 1) the magnetic vector potential  $\vec{A}$  generated by a transmitter coil is equal to the primary vector potential  $\vec{A}_p$ , which exists in the absence of the conductive body and 2) the displacement currents are negligible. Thus, the vector potential term in the electric field expression can easily be calculated for a certain coil configuration. Calculation of the scalar potential distribution for the same coil configuration requires the solution of the following differential equation [13], [14]:

$$\begin{aligned} \nabla \cdot (\sigma \nabla \phi) &= -\omega \vec{A}_p \cdot \nabla \sigma \\ \frac{\partial \phi}{\partial n} &= \omega A_{pn} \end{aligned} \quad (2)$$

where  $A_{pn}$  is the normal component of the magnetic vector potential on the surface of the conductive body. Here, for notational simplicity,  $\phi$  represents the imaginary component of the scalar potential since the real part is zero [14]. Thus, the electric field can now be expressed as  $\vec{E} = -j(\omega\vec{A} + \nabla\phi)$ . After solving for the scalar potential, the induced current density  $\vec{J}_i$  in the conductive body can be obtained by  $\vec{J}_i = \sigma\vec{E}$ . Formulation of the forward problem simply continues by applying Biot–Savart law, using the two current components: 1) the current in the transmitter coil ( $\vec{J}_T$ ) and 2) the induced currents in the conductive body ( $\vec{J}_i$ ). Note that there is a 90° phase difference between these two currents. The magnetic

flux density  $\vec{B}$  is then

$$\vec{B} = \frac{\mu_0}{4\pi} \int \vec{J}_T \times \frac{\vec{R}}{R^3} dV_{\text{coil}} + \frac{\mu_0}{4\pi} \int \vec{J}_i \times \frac{\vec{R}}{R^3} dV_{\text{body}} \quad (3)$$

or

$$\vec{B} = \vec{B}_p + \vec{B}_s$$

where  $\vec{B}_p$  and  $\vec{B}_s$  represent the primary and secondary magnetic fields, respectively. Here,  $\vec{B}_s$  can be expressed more explicitly

$$\vec{B}_s = -j \frac{\mu_0}{4\pi} \int \sigma (\omega \vec{A}_T + \nabla\phi) \times \frac{\vec{R}}{R^3} dV_{\text{body}} \quad (4)$$

where  $\mu_0$  is the free-space permeability and  $\vec{R}$  represents the vector from the source point in the conductive body to the field point ( $R$  is the distance between these points).

Note that the relation between  $\vec{B}_s$  and  $\sigma$  is a rather complicated mapping since  $\nabla\phi$ , itself, depends on conductivity. However, a first-order variation in the secondary magnetic fields  $\Delta\vec{B}_s$ , related to the perturbation  $\Delta\sigma$  in the conductivity distribution, can be determined. If  $\vec{B}_s$  and  $\vec{B}_{s0}$  are the magnetic flux densities corresponding to  $\sigma$  and  $\sigma_0$ , then (4) can be rewritten by substituting  $\phi_0 + \Delta\phi$  and  $\sigma_0 + \Delta\sigma$  for  $\phi$  and  $\sigma$ , as shown in (5) at the bottom of this page. The last term in the right-hand side can be neglected, since it is a second-order variation. The first term is  $\vec{B}_{s0}$ , so it may be taken to the left-hand side, yielding  $\Delta\vec{B}_s = \vec{B}_s - \vec{B}_{s0}$ . The second term can be rewritten by replacing  $\nabla(\Delta\phi)$  with  $(\partial(\nabla\phi)/\partial\sigma)\Delta\sigma$ . Consequently, we obtain the following expression relating the variation in the secondary magnetic fields to the conductivity perturbation:

$$\begin{aligned} \Delta\vec{B}_s &= -j \frac{\mu_0}{4\pi} \left[ \int \frac{\vec{R}}{R^3} \times \left( \omega \vec{A}_T + \nabla\phi_0 + \sigma_0 \frac{\partial(\nabla\phi)}{\partial\sigma} \right) \right. \\ &\quad \left. \times \Delta\sigma dV_{\text{body}} \right]. \end{aligned} \quad (6)$$

### B. Measurement Sensitivity to Conductivity Distribution

Let us assume that excitation and detection coils are located above the conducting object, as shown in Fig. 3. Using the magnetic reciprocity theorem [36], it is possible to obtain the flux  $\Phi$  in the detector coil as follows:

$$\Phi = \frac{1}{I_R} \int \vec{A}_R \cdot \vec{J} dV \quad (7)$$

$$\begin{aligned} \vec{B}_s &= -j \frac{\mu_0}{4\pi} \int (\sigma_0 + \Delta\sigma) (\omega \vec{A}_T + \nabla(\phi_0 + \Delta\phi)) \frac{\vec{R}}{R^3} dV_{\text{body}} \\ &= -j \frac{\mu_0}{4\pi} \left[ \int \sigma_0 (\omega \vec{A}_T + \nabla\phi_0) \times \frac{\vec{R}}{R^3} dV_{\text{body}} \right. \\ &\quad + \int \sigma_0 \nabla(\Delta\phi) \times \frac{\vec{R}}{R^3} dV_{\text{body}} + \int \Delta\sigma (\omega \vec{A}_T + \nabla\phi_0) \\ &\quad \left. \times \frac{\vec{R}}{R^3} dV_{\text{body}} + \int \Delta\sigma \nabla(\Delta\phi) \times \frac{\vec{R}}{R^3} dV_{\text{body}} \right]. \end{aligned} \quad (5)$$

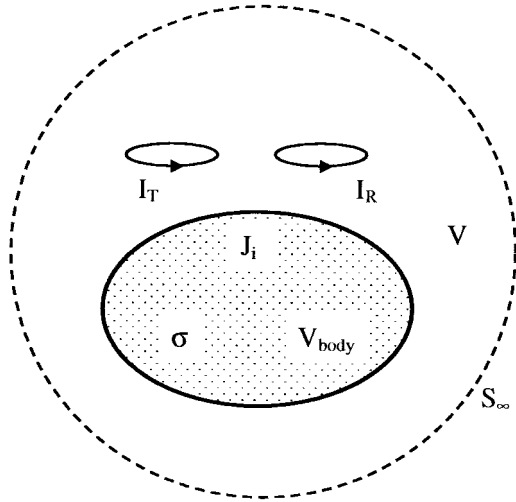


Fig. 3. Relation between the magnetic flux densities generated by current  $I_T$  in the transmitter coil and the reciprocal current  $I_R$  in the detector coil.

where  $\vec{A}_R$  is the magnetic vector potential created by the reciprocal current  $I_R$  in the detector coil. Here,  $\vec{J}$  is equal to  $\vec{J}_T$  in the excitation coil volume and  $\vec{J}_i$  in the conductive body. Consequently, the flux in the detector coil is obtained by taking the integrals in the corresponding volumes

$$\Phi = \frac{1}{I_R} \oint \vec{A}_R \cdot \vec{J}_T dV_{\text{coil}} + \frac{1}{I_R} \int \vec{A}_R \cdot \vec{J}_i dV_{\text{body}}. \quad (8)$$

The first term on the right is the primary flux, directly coupled from the transmitter coil. The second term represents the flux caused by the induced currents. The electromotive force  $v$  in the receiver coil can be expressed as

$$\begin{aligned} v &= -j\omega\Phi \\ &= -j \left( I_T \oint \left( \frac{\omega \vec{A}_R}{I_R} \right) \cdot d\vec{l} \right) - \int \left( \frac{\omega \vec{A}_R}{I_R} \right) \\ &\quad \cdot \sigma (\omega \vec{A}_T + \nabla\phi) dV'. \end{aligned} \quad (9)$$

Here, the term  $-\omega \vec{A}_R / I_R$  (the magnetic lead field) represents the electric field that can be created by the detector coil, energized with unit reciprocal current. The two terms in the right-hand side represent the primary ( $v_p$ ) and secondary ( $v_s$ ) voltages, respectively.

### C. Numerical Formulation and Solution of the Forward Problem Using the FEM

Analytical solutions for the secondary magnetic field are available for special conductive body geometries. An example for such a solution is provided by [4] and is given in the Appendix. However, for a general conductivity distribution  $\sigma$ , solutions for the secondary magnetic field can not be obtained by analytical methods. Equation (4) gives the general relation between the measurements and induced currents. In order to calculate the secondary magnetic fields, due to induced currents in an arbitrary conductivity distribution, the scalar potential distribution  $\phi$  should be solved. In this study,  $\phi$  is obtained using the FEM.

For the FEM formulation, the conductive body is divided into volume elements (voxels). On each element, the conductivity is taken to be constant and  $\phi$  is approximated by a summation of simple functions and the scalar potentials of the nodes are unknowns. If  $\vec{V}$  denotes the vector of unknown scalar potentials at the nodes, the following matrix equation is obtained:

$$\mathbf{A}(\vec{\sigma})\vec{V} = \vec{b}(\vec{\sigma}) \quad (10)$$

where  $\vec{\sigma}$  denotes the vector of element conductivities,  $\vec{b}$  is the vector incorporating interface conditions, as well as boundary conditions. Here,  $\mathbf{A}(\vec{\sigma})$  is a sparse matrix whose entries depend on the element geometries and element conductivities. Tests for simple body geometries showed that FEM solutions of the scalar potential  $\phi$  have a peak error of less than 1% when compared with analytical solutions [16], [17]. After solving scalar potential  $\phi$  for each node, it is possible to find  $\nabla\phi$  and  $\partial(\nabla\phi)/\partial\sigma$  at any point in the conductive body, using standard tools developed for the implementation of the FEM. Consequently,  $\vec{B}_s$  and  $\Delta\vec{B}_s$  can be calculated, using (4) and (6), for a given initial conductivity distribution.

If the conductive body is divided into  $n$  voxels, then (6) can be rewritten as a summation across these  $n$  elements. For example, for the  $i$ th measurement it is possible to express  $\Delta\vec{B}_{si}$  as

$$\Delta\vec{B}_{si} = \sum_{j=1}^n r_{ij} \Delta\sigma_j$$

where

$$r_{ij} = \int \frac{\vec{R}_{ij}}{R_{ij}^3} \times \left( \omega \vec{A}_{Tj} + \nabla\Phi_{0j} + \frac{\partial(\nabla\phi)}{\partial\sigma_j} \right) dV_j.$$

Here, the subscript  $j$  denotes that the parameter is evaluated on the  $j$ th element.

Let there be  $m$  field points, then the following matrix equation relates the perturbation in conductivity  $\Delta\vec{\sigma}$  to the perturbation in magnetic fields  $\Delta\vec{B}_s$ :

$$\Delta\vec{B}_s = \mathbf{S}\Delta\vec{\sigma} \quad (11)$$

where  $\Delta\vec{B}_s$  is an  $m \times 1$  vector of measurements,  $\Delta\vec{\sigma}$  is  $n \times 1$  vector of conductivity perturbations, and  $\mathbf{S}$  is an  $m \times n$  sensitivity matrix.

The sensitivity matrix can also be calculated using a different method. In that method, the secondary magnetic fields are calculated twice for each excitation. In the first calculation, an initial estimate is used for the conductivity distribution of the body. In the second case, the conductivity of a single voxel is perturbed by, for example, 1% of the voxel's initial estimate. For a particular field point, the difference of the calculated fields divided by the variation in voxel conductivity, provides the sensitivity of that measurement to the change in the voxel conductivity. The calculation of the sensitivity matrix using this method requires a considerable amount of time and, thus, it is not used in this study.

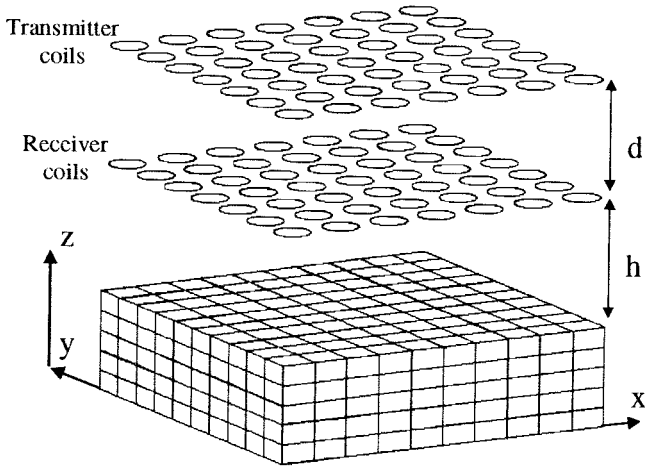


Fig. 4. A cubic conductive body with dimensions  $10 \times 10 \times 5$  cm. Each voxel in the FEM mesh is  $1 \times 1 \times 1$  cm. All coils have radii of 0.5 cm. Receiver coils are located 0.5 cm above conductive body ( $h = 0.5$  cm). Transmitter coil plane lies 0.5 cm above receiver coil plane ( $d = 0.5$  cm). Note that the scales are exaggerated to ease display.

### III. THE INVERSE PROBLEM

#### A. Properties of the Sensitivity Matrix

In order to understand the imaging capability of the proposed system, the properties of the sensitivity matrix should be investigated. For that purpose, a body geometry and a coil configuration must be specified. In this study, the conductive body is chosen as  $10 \times 10 \times 5$ -cm cubic object which has a uniform conductivity of 0.2 S/m (Fig. 4). The body is divided into  $1 \times 1 \times 1$ -cm volume elements, yielding 500 voxels. A  $7 \times 7$  grid of coils covers the top surface of the conductive body. Both the excitation and recording coils have a radii of 0.5 cm and 1000 turns. The excitation coil carries a sinusoidal current of 1 A at 50 kHz. The transmitter and receiver coil planes are located at 1- and 0.5-cm distance from the top surface of the body, respectively. For each excitation, one of the 49 transmitter coils is energized to induce current in the conductive medium and 49 measurements are obtained. When this scheme is repeated for all transmitter coils, it is possible to obtain  $2401 (= 49 \times 49)$  measurements. Thus, the sensitivity matrix  $\mathbf{S}$  is of dimension  $2401 \times 500$ .

Rows of  $\mathbf{S}$  are displayed to understand the sensitivity of measurements to voxel conductivity perturbations. Fig. 5 shows the sensitivity distribution for a selected drive-measurement coil pair. Note that sensitivity to conductivity perturbations is high for voxels beneath the transmitter and receiver coils. Sensitivity is also high for voxels between these coils.

Singular-value decomposition (SVD) of  $\mathbf{S}$  provides the singular values, the basis vectors of the measurement, and image domains (right and left singular vectors). The normalized singular values of the sensitivity matrix are provided in Fig. 6. The condition number is calculated as  $7.41 \times 10^6$ . The image domain singular vectors are also displayed to understand the characteristics of the imaging system. It is observed that singular vectors which correspond to smaller singular values include high-frequency conductivity variations at distant points from the coil locations.

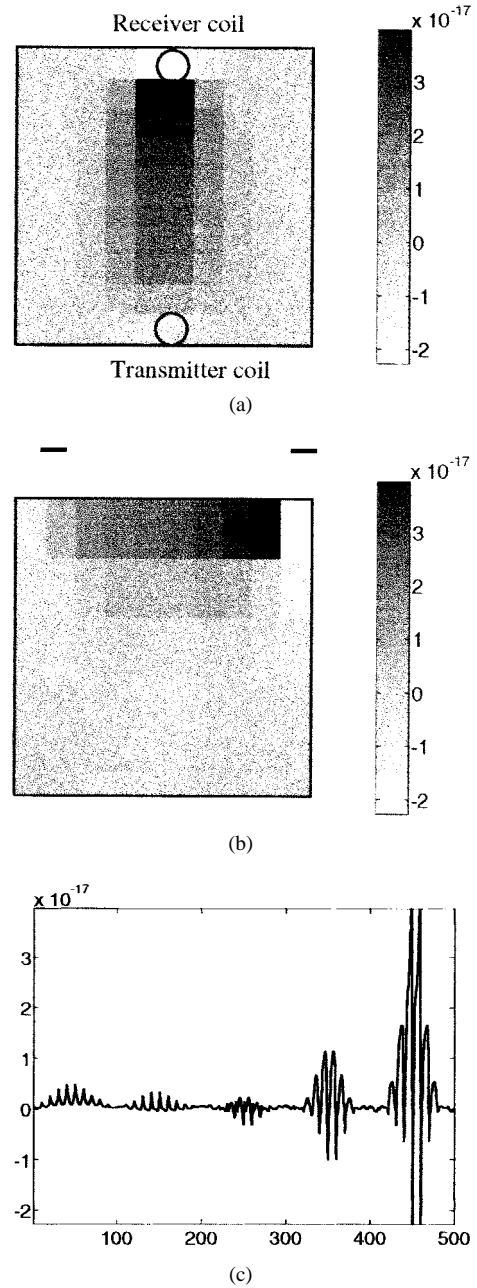


Fig. 5. Plot of the sensitivity pattern for the selected transmitter–receiver coil pair. (a)  $x$ - $y$  plane at  $z = 5$  cm. (b)  $y$ - $z$  plane (which intersects the coil centers). (c) One-dimensional plot of sensitivity distribution.

#### B. Image Reconstruction

Images of conductivity distribution are obtained using the Newton–Rampson Method. This is achieved by first linearizing the forward problem around an initial conductivity estimate  $\bar{\sigma}_0$ , as given in (6), and obtaining the matrix equation (11). The minimum-norm least squares (MNLS) solution to  $\Delta\bar{\sigma}$  is found by pseudoinverse of  $\mathbf{S}$  (denoted by  $\mathbf{S}^\dagger$ ) as

$$\Delta\bar{\sigma} = \mathbf{S}^\dagger \Delta\bar{\mathbf{B}}. \quad (12)$$

(Calculation of pseudoinverse using SVD is given in the Appendix.) This process continues by updating the voxel conductivities by  $\bar{\sigma} = \bar{\sigma}_0 + \Delta\bar{\sigma}$  and calculating the sensitivity matrix for the new conductivity distribution to form the new matrix equation, as given in (11).

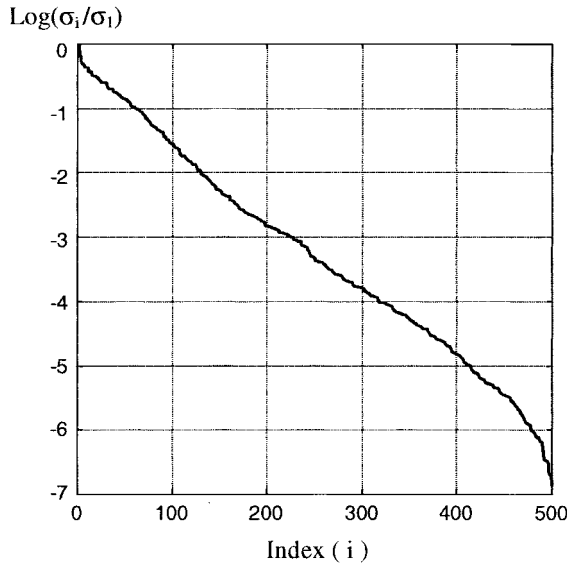


Fig. 6. Singular-value plot of the sensitivity matrix. All singular values are normalized with the maximum singular value ( $3.57 \times 10^{-14}$ ) and logarithms of the normalized singular values are plotted.

Images are reconstructed, using simulated data obtained for different conductivity distributions. The measurement data set is obtained by solving the induced currents for each excitation coil location and calculating the secondary magnetic fields, using (4). The above image-reconstruction process starts, using an initial estimate for conductivity distribution and calculating the secondary magnetic fields for this estimate.

The performance of the new imaging system can be assessed by calculating the point-spread function (PSF), using single voxel perturbations. However, obtaining and visualizing images for each voxel perturbation is a tedious work. Instead, we prefer to use the resolution matrix concept to provide the results of all such simulations. Let  $\Delta\bar{\sigma}^*$  represent the MNLS image of the actual conductivity perturbation  $\Delta\bar{\sigma}$ , then

$$\Delta\bar{\sigma}^* = \mathbf{S}^\dagger \Delta\bar{\mathbf{B}} = \mathbf{S}^\dagger \mathbf{S} \Delta\bar{\sigma}. \quad (13)$$

Use of SVD for defining  $\mathbf{S}$  and  $\mathbf{S}^\dagger$  leads to the following:

$$\Delta\bar{\sigma}^* = \mathbf{V}\mathbf{V}^T \Delta\bar{\sigma} = \mathbf{R} \Delta\bar{\sigma} \quad (14)$$

where  $\mathbf{V}$  is an  $n \times m$  matrix that includes the right singular vectors (image basis vectors) as its columns and  $\mathbf{R} = \mathbf{V}\mathbf{V}^T$  is an  $n \times n$  matrix, namely, the resolution matrix. Each column or row of  $\mathbf{R}$  is the image of a single voxel perturbation, reconstructed by the described imaging system. Once  $\mathbf{R}$  is stored, simulation studies for different  $\Delta\bar{\sigma}$  can be carried out without even making forward and inverse transformations. Note that when the number of basis vectors is equal to the number of unknowns, then  $\mathbf{R}$  becomes an identity matrix. This means that, using such a system, any perturbation can be identically reconstructed. However, the number of image basis vectors used in image reconstruction may change according to the noise level in the measurements (see the Appendix for the definition of the truncated pseudoinverse). If this number is  $r < n$ , then  $\mathbf{V}$  will be an  $n \times r$  matrix and the characteristics of matrix  $\mathbf{R}$  changes according to the number of truncated basis

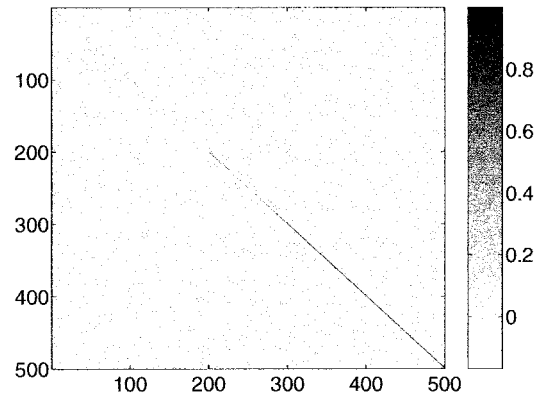


Fig. 7. Resolution matrix of the 49-coil system. There are 100 voxels on each layer. The voxels on the uppermost layer (center of voxels are at  $x$ - $y$  plane where  $z = 4.5$  cm) are indexed as 401–500, the voxels in the next layer are indexed as 301–400, and so on.

vectors. The resolution matrix of the described system is obtained using 300 basis vectors in  $\mathbf{V}$ , assuming a possible SNR of 80 dB and displayed in Fig. 7. Note that in the bottom right corner the matrix is diagonal and the diagonal entries are unity. This shows that the imaging system can perfectly reconstruct the corresponding single-voxel perturbations. This behavior can be observed even for voxels at a depth of 2 cm. For deeper voxels, a spread should be observed. Fig. 8 shows the reconstructed images to demonstrate this depth dependency. For that purpose, a voxel is selected at the center of each layer. Thereafter, the corresponding rows of  $\mathbf{R}$  are displayed as a one-dimensional (1-D) function in the right-hand side. This gives the overall amplitude variation in the reconstructed 3-D image. The image of the related layer is also displayed in the left-hand side to show the spread in the selected slice. It is observed that the resolution in the reconstructed images decreases as the distance of the voxel from the measurement surface increases. There is also a considerable spread in the image toward the upper and lower layers.

#### IV. CONCLUSIONS AND DISCUSSIONS

In this study, the forward and inverse problems of a new medical-imaging modality were discussed in detail. The ultimate aim of this new modality is to reconstruct electrical conductivity images of biological tissues via contactless measurements. This is achieved by applying time-varying magnetic fields to induce currents in the conductive body. Thereafter, the magnetic fields of the induced currents are measured and used to image conductivity distribution.

The forward problem of the imaging system was defined as a calculation of the secondary magnetic fields, due to the induced current components in the medium. The induced currents were expressed using the  $\vec{A}$ - $\phi$  formulation of the electric field (i.e.,  $\vec{E} = -j\omega\vec{A} - \nabla\phi$ ). It was assumed that  $\vec{A}$  describes the primary magnetic field in the absence of the body. In order to solve the scalar potential distribution for objects of arbitrary conductivity distribution a 3-D FEM formulation was employed. The secondary magnetic field expression was linearized around an initial conductivity distribution. In discretized form, a linear system of equations was obtained,

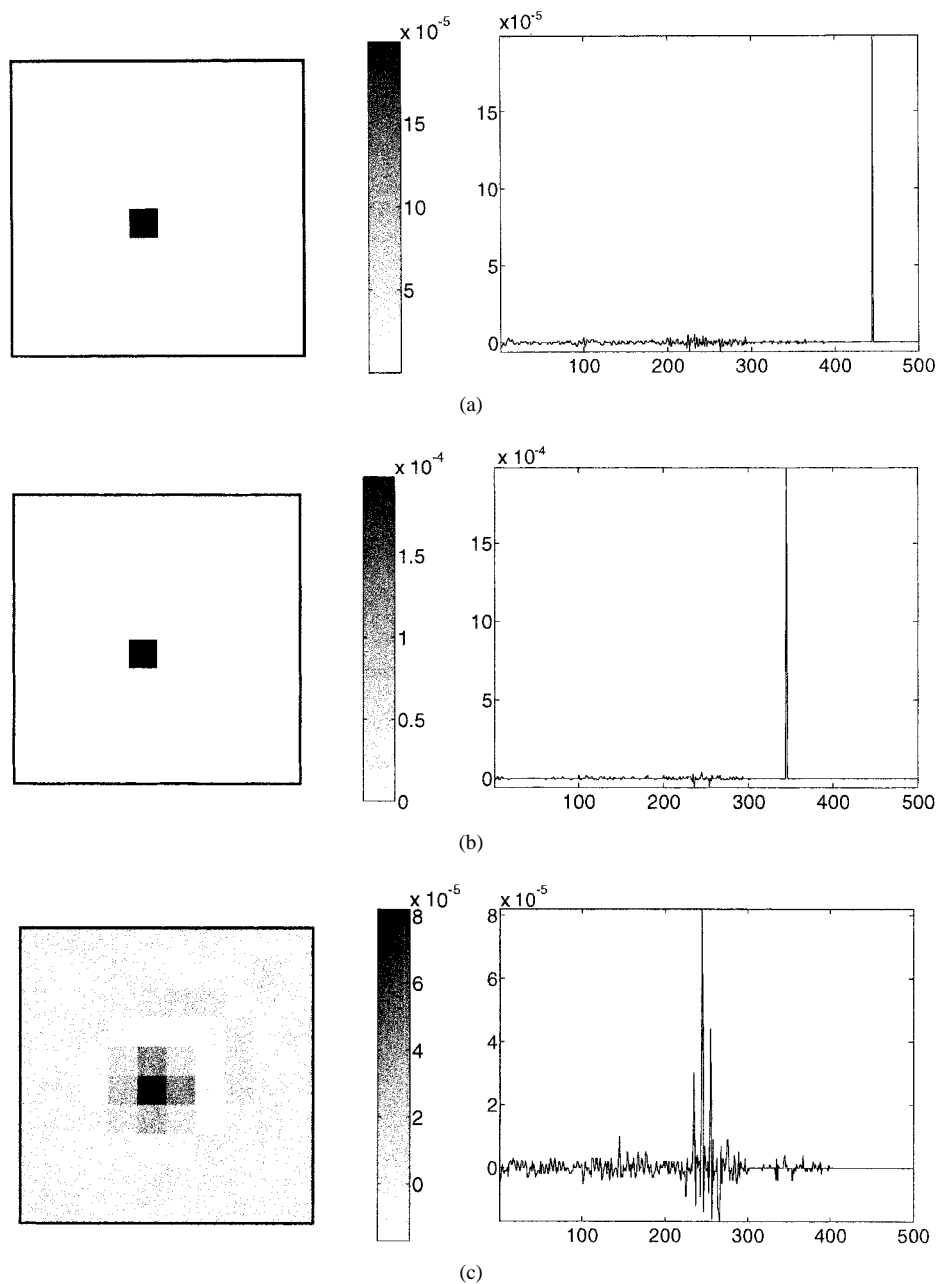


Fig. 8. The reconstructed images of single-voxel perturbations. The voxels are selected at the centers of each layer. One-dimensional plot of all voxels is shown on the left and the image of perturbed layer is shown on the right. The  $z$  coordinate of the center of the selected voxel is: (a)  $z = 0.5$  cm, (b)  $z = 1.5$  cm, and (c)  $z = 2.5$  cm.

relating the perturbations in magnetic field measurements to the conductivity perturbations. Assuming an array of coaxial coils near the top surface of a conductive body, the sensitivity matrix  $\mathbf{S}$  was calculated and its properties were discussed. It was shown that the sensitivity to deeper regions gradually decreases. The SVD of  $\mathbf{S}$  showed that the condition number is high. The reason was the low measurement sensitivity to high-frequency oscillations of the conductivity perturbations in the deeper regions of the conductive body. This affected the images reconstructed with additive measurement noise. Thus, truncated pseudoinverse solutions were obtained, sacrificing the resolution in depth.

In practice, the body geometry used in the numerical model may not fit the actual geometry. The variation in the distance

between the transmit/receive coils and the skin surface may cause significant differences between the measured and the calculated fields and undesirable results in the reconstructed images. In the case of complicated body geometries, such as the human head, it is possible to avoid such artifacts by taking MRI's of the subject with markers to provide the required coordinate system. Thereafter, segmentation and surface reconstruction algorithms can be applied to parameterize the body surface.

In the calculation of induced currents, two components of the electric field were taken into account. The  $\sigma\omega\vec{A}_T$  term is linearly related to the conductivity distribution. However, the second term,  $\sigma\nabla\phi$ , introduces nonlinearity as  $\phi$  itself is a function of conductivity. An alternative strategy, that

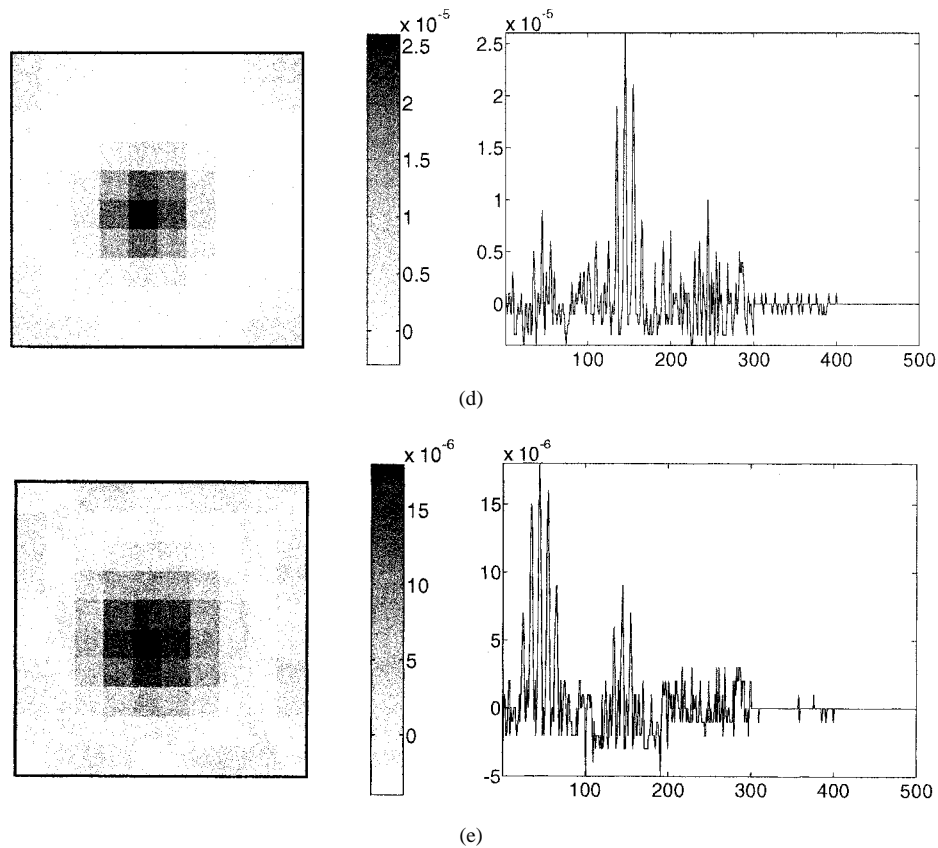


Fig. 8. (Continued.) The reconstructed images of single-voxel perturbations. The voxels are selected at the centers of each layer. One-dimensional plot of all voxels is shown on the left and the image of perturbed layer is shown on the right. The  $z$  coordinate of the center of the selected voxel is: (d)  $z = 3.5$  cm and (e)  $z = 4.5$  cm.

was not applied in this study, is to find an initial estimate of the conductivity distribution by neglecting the nonlinear component of induced currents. This might provide an easy and quick way of obtaining an initial estimate. Since the magnetic vector potentials can easily be calculated for a given coil configuration, this process does not require cumbersome numerical work. However, neglecting the nonlinear term might introduce large errors, especially at the inner conductivity interfaces and body surface. The possible advantages of such a methodology will be revealed in future studies.

The degree of nonlinearity is analyzed by reconstructing images for higher conductivity perturbations. Even for conductivity perturbations of 50% of the background conductivity, it is possible to reconstruct images that are indicative of the inhomogeneity.

In this study, a new method is described to obtain the sensitivity matrix. The time required to obtain the sensitivity matrix is 1609 min in a 166-MHz PC with a memory of 128 MB. Note that the new method provides a considerable reduction in the computation time, compared to the method based on solutions of the forward problem.

The possible applications of the proposed technique are those that were originally studied for injected-current electrical-impedance imaging. However, the properties of the data acquisition system will be different, depending on the selected application. For static images, it may be feasible to obtain one image per hour. For cardiac-related images, Eyuboglu *et al.* had collected 20 frames (the complete set of

data to obtain an image) from the thorax at a rate of ten frames per second with ACEIT [22]. Smith *et al.* had realized a real-time impedance imaging system which collects 25 frames/s [27]. The feasibility of such rates for the proposed technique depends on a number of parameters (the  $S/N$  achieved, the number of receiver coils, depth of conductivity changes, etc.) and should be further studied, depending on the selected application.

In the simulated imaging experiments of this study, the average, maximum, and minimum of the secondary emf at the receiving coils are 28, 82, and  $5 \mu\text{V}$ , respectively. The available emf shows us that modern lock-in amplifiers with sensitivity on the order of nanovolts can be used to obtain measurements. However, error sources and other limitations on the measurement technique should be revealed by further studies on data acquisition.

In conclusion, this study forms a mathematical basis for the future developments in electrical conductivity imaging via contactless measurements. The mathematical tools of this study can be used to improve the performance of the imaging system, for example, by exploring the use of different excitation types and multifrequency excitations.

## APPENDIX

### A. Analytical Solutions for Layered Conductive Half Space

Wait has derived a very useful formulation for multilayer half-space earth, excited by a circular coil located in the

air (Fig. 2), for the purpose of geophysical exploration [4]. Once the basic assumptions are satisfied, the same formulation can be used to understand the feasibility of the measurement technique to explore the conductivity of biological tissues. This can be done by assigning tissue conductivities to the layers.

Let  $\omega$  represent the operation frequency and  $k_1 = j\omega\mu_0\sigma_1$  and  $k_2 = j\omega\mu_0\sigma_2$ , then using the following assumptions, it is possible to obtain relatively simple expressions: 1) the displacement currents are negligible; 2) the coil radius is much smaller than the distance  $R$  between the transmitter and receiver coils (so that it can be represented as a magnetic dipole); and 3)  $|k_1R|^2$  and  $|k_2R|^2$  are much less than one. Consequently, the primary and secondary magnetic flux densities are

$$\begin{aligned} B_x^p &= 3Cx(z-h)/R^5 \\ B_y^p &= 3Cy(z-h)/R^5 \\ B_z^p &= 3C(z-h)^2/R^5 - C/R^3 \\ B_x^s &= -Ct_1(x/r) \\ B_y^s &= -Ct_1(y/r) \\ B_z^s &= -Ct_0 \end{aligned}$$

where  $R = (r^2 + (z-h)^2)^{1/2}$ ,  $C = I\mu_0 dA/4\pi$ , and  $dA = \pi a^2$  is the infinitesimal area of the coil. The parameters  $t_0$  and  $t_1$  are defined as the following:

$$\begin{aligned} t_0 &= \frac{k_1^2}{4} \left\{ \frac{1}{[r^2 + (z+h)^2]^{1/2}} - \frac{1}{[r^2 + (2d+z+h)^2]^{1/2}} \right\} \\ &\quad + \frac{k_2^2}{4} \left\{ \frac{1}{[r^2 + (2d+z+h)^2]^{1/2}} \right\} \\ t_1 &= \frac{k_1^2}{4r} \left\{ \frac{2d+z+h}{[r^2 + (2d+z+h)^2]^{1/2}} - \frac{z+h}{[(2d+z+h)^2]^{1/2}} \right\} \\ &\quad - \frac{k_2^2}{4r} \left\{ \frac{z+h}{[(2d+z+h)^2]^{1/2}} \right\}. \end{aligned} \quad (15)$$

In the following two subsections, expressions for the voltages in the receiver coil, due to the current  $I$  in the transmitter coil, will be presented for two types of coil configurations given in Fig. 2 [4]: 1) coplanar coils with axes vertical to the half space and 2) coaxial coils with axes vertical to the half space.

1) *Coplanar Coils with Axes Vertical to the Half Space:* Let the transmitter coil area, the number of turns, and the coil current be denoted by  $S_1$ ,  $N_1$ , and  $I$ , respectively. Since both coils are at the same height ( $z = h$ ), the first term of the primary magnetic-flux density  $B_z^p$  is zero. Thus,  $B_z^p$  at a distance  $r$  is

$$B_{z, \text{copl}}^p = -\frac{\mu_0 I N_1 S_1}{4\pi r^3}. \quad (16)$$

The primary voltage  $v_p$  induced in a  $N_2$ -turn receiver coil of area  $S_2$  is

$$v_p = -j\omega B_{z, \text{copl}}^p \times N_2 S_2 \quad (17)$$

or

$$v_p = j\omega\mu_0 \frac{I(N_1 S_1) \times (N_2 S_2)}{4\pi r^3}. \quad (18)$$

The secondary voltage  $v_s$  can be calculated by first noting that

$$B_z^s = -(\mu_0 I N_1 S_1 / 4\pi) \times t_0$$

then

$$v_s = -j\omega B_z^s \times N_2 S_2 \quad (19)$$

or

$$v_s = j\omega\mu_0 \frac{I(N_1 S_1) \times (N_2 S_2)}{4\pi} \times t_0 = v_p r^3 \times t_0 \quad (20)$$

then the total voltage  $v$  is

$$v = v_p(1 + r^3 t_0). \quad (21)$$

2) *Coaxial Coils with Axes Vertical to the Half Space:* The primary magnetic field  $B_{z, \text{coax}}^p$  at a distance  $d$  from the transmitter coil center is

$$B_{z, \text{coax}}^p = \frac{\mu_0 I N_1 S_1}{2\pi(a^2 + d^2)^{3/2}}. \quad (22)$$

The primary voltage  $v_p$  induced in a  $N_2$ -turn receiver coil of area  $S_2$  is

$$v_p = -j\omega B_{z, \text{coax}}^p \times N_2 S_2 \quad (23)$$

or

$$v_p = -j\omega\mu_0 \frac{I(N_1 S_1) \times (N_2 S_2)}{2\pi(a^2 + d^2)^{3/2}}. \quad (24)$$

The secondary voltage is in the following form:

$$\begin{aligned} v_s &= \frac{1}{4\pi} j\omega\mu_0 (N_1 S_1) \times (N_2 S_2) \times t_0 \\ &= -\frac{1}{2} v_p (a^2 + d^2)^{3/2} \times t_0. \end{aligned} \quad (25)$$

Thus, the total pickup voltage is

$$v = v_p \left[ 1 - \frac{1}{2} (a^2 + d^2)^{3/2} \times t_0 \right].$$

## B. FEM Formulation

In this study, the FEM is used to solve the scalar potential distribution  $\phi$  in objects of arbitrary conductivity distribution. The body conductivity is assumed to be isotropic. The FEM formulation for anisotropic conductivity distributions is given in [17].

The FEM formulation is performed for 20 noded isoparametric quadratic hexahedral elements (Fig. 9). Applying Galerkin's weighted residuals method to the partial differential equation (2)

$$\int N_i \nabla \cdot (\sigma_e \nabla \phi) dV_e = - \int N_i \nabla \sigma \cdot \omega \vec{A} dV_e \quad (26)$$

is to be satisfied for each quadratic shape function,  $i = 1 \dots 20$  [14]. In all equations, subscript  $e$  is used to show that integrations are taken on element volume and surface. Assuming constant conductivity in each element ( $\nabla \sigma = 0$ ), the previous equation becomes

$$\int N_i \nabla \cdot (\sigma_e \nabla \phi) dV_e = 0 \quad (27)$$

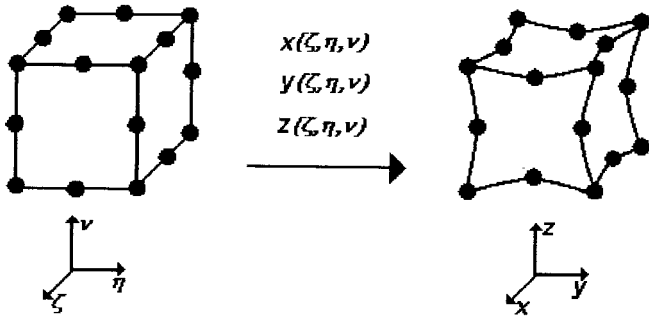


Fig. 9. 20-noded hexahedral elements. Quadratic variations are supported on the edges of this element. Unit element in local coordinates is on the left. A possible element in global coordinates is on the right.

which can be rewritten as

$$\int \nabla \cdot (N_i \sigma_e \nabla \phi) dV_e - \int \sigma_e \nabla N_i \cdot \nabla \phi dV_e = 0. \quad (28)$$

Using the divergence theorem and  $\nabla \phi \cdot \vec{n} = -\omega \vec{A} \cdot \vec{n}$  on every element surface, we obtain

$$\int \sigma_e \nabla N_i \cdot \nabla \phi dV_e = - \int N_i \sigma_e \omega \vec{A} \cdot d\vec{S}_e. \quad (29)$$

$\phi$  and  $\nabla \phi$  are expressed in an element as

$$\phi = \sum_{i=1}^{20} N_i \phi_i \quad (30)$$

$$\nabla \phi = \sum_{i=1}^{20} \nabla N_i \phi_i. \quad (31)$$

Placing (31) in (29) we obtain an equation in terms of the node potentials  $\phi_i$ . Repeating this process for  $i = 1 \dots 20$ , an element matrix equation can be formed. After an assembly process, a matrix equation relating the unknown node potentials to the excitation parameters is obtained. In matrix form

$$\mathbf{A}(\vec{\sigma}) \vec{\mathbf{V}} = \vec{\mathbf{b}}(\vec{\sigma}). \quad (32)$$

Since  $\mathbf{A}(\vec{\sigma})$  is large in dimension but sparse, solution of  $\vec{\mathbf{V}}$  is obtained by a conjugate transpose solver [37]. Numerical surface and volume integrations are evaluated by 9- and 27-point Gauss–Legendre quadrature integration procedures, respectively.

### C. SVD and Pseudoinverse Solutions

For an  $m \times n$  matrix  $\mathbf{A}$  there exist orthogonal matrices [38]

$$\begin{aligned} \mathbf{U} &= [\mathbf{u}_1, \dots, \mathbf{u}_m] \\ \mathbf{V} &= [\mathbf{v}_1, \dots, \mathbf{v}_n] \end{aligned}$$

such that

$$\mathbf{U}^T \mathbf{A} \mathbf{V} = \mathbf{D} = \text{diag}(\sigma_1, \dots, \sigma_p) \quad p = \min(m, n)$$

where

$$\sigma_1 \geq \sigma_2 \geq \dots \geq \sigma_p \geq 0 \quad (33)$$

and  $\sigma_i$  are the singular values of  $\mathbf{A}$ . The matrix  $\mathbf{D}$  is a diagonal matrix with the singular values on its main diagonal.

Furthermore, if  $\text{rank}(\mathbf{A}) = r$ , i.e.,

$$\sigma_1 \geq \dots \geq \sigma_r > \sigma_{r+1} = \dots = \sigma_p = 0$$

then the SVD expansion [38] is defined by

$$\mathbf{A} = \mathbf{U}_r \mathbf{\Sigma}_r \mathbf{V}_r^T = \sum_{i=1}^r \sigma_i \mathbf{u}_i \mathbf{v}_i^T \quad (34)$$

where the vectors  $\mathbf{u}_i$  and  $\mathbf{v}_i$  are the  $i$ th left and right singular vectors of dimension  $m \times 1$  and  $n \times 1$ , respectively.  $\mathbf{U}_r$  and  $\mathbf{V}_r$  are  $m \times r$  and  $n \times r$  matrices composed of the related  $r$  singular vectors and  $\mathbf{\Sigma}_r$  is the  $r \times r$  diagonal matrix with the first  $r$  singular values on the main diagonal.

The MNLS solution to a linear system of equations can be obtained by the Moore–Penrose Inverse [39], [40] or pseudoinverse of  $\mathbf{A}$  defined by

$$\mathbf{A}^\dagger = \sum_{i=1}^r \frac{1}{\sigma_i} \mathbf{v}_i \mathbf{u}_i^T. \quad (35)$$

If the noise  $\mathbf{n}$  in the measurements is additive, then the MNLS solution will be [41], [42]

$$\hat{\mathbf{x}} = \mathbf{A}^\dagger (\mathbf{s} + \mathbf{n}) \quad (36)$$

$$= \sum_{i=1}^r x_i \mathbf{v}_i + \sum_{i=1}^r \frac{1}{\sigma_i} n_i \mathbf{v}_i \quad (37)$$

where

$$\begin{aligned} x_i &= \frac{1}{\sigma_i} (\mathbf{u}_i^T \mathbf{s}) = \mathbf{v}_i^T \mathbf{x} \\ n_i &= (\mathbf{u}_i^T \mathbf{n}). \end{aligned}$$

In such a case, the condition number of the matrix  $\mathbf{A}$  (the ratio of maximum to minimum singular values) and the noise level in the measurements becomes important. The second term of (37) may dominate the first term because of the small singular values. The noise level in the measurements must be sufficiently small to compensate for the effects of the smallest singular values. For cases where this is not possible, the effects of the second term can be eliminated by using the method of the truncated pseudoinverse, described in [41]. This method is simply carried out by truncating at an earlier index  $p < r$  in the evaluation of  $\mathbf{A}^\dagger$  given by (35). However, while this method reduces the effects of measurement noise on the reconstructed images, it also imposes a severe loss of information because of the exclusion of image components. The optimal truncation index  $p_{\text{opt}}$  is found as

$$p_{\text{opt}} = \max_k \left\{ k \left| \frac{\sigma_k^2}{\sigma_1^2} \geq \frac{E(\|\mathbf{n}\|^2)}{E(\|\mathbf{s}\|^2)} \right. \right\} \quad (38)$$

assuming  $\mathbf{x}$  and  $\mathbf{n}$  are independent white Gaussian vectors [41], [43], [44]. The operators  $E(\cdot)$  and  $\|\cdot\|$ , respectively, represent the expected value and the Euclidean norm operations. The SNR of a data acquisition system can be defined as

$$\text{S/N} = 10 \log \frac{E(\|\mathbf{s}\|^2)}{E(\|\mathbf{n}\|^2)} \quad (39)$$

where the ratio of expected values is equivalent to the ratio of the variances of the measurements and noise. Consequently,

SNR's of 40 and 20 dB correspond to norm ratios of 100 and 10, respectively. The singular value at the truncation level is the smallest singular value that satisfies the following inequality:

$$20 \log \frac{\sigma_1}{\sigma_k} \leq S/N \quad k = 1, \dots, r. \quad (40)$$

#### REFERENCES

- [1] J. P. Morucci and B. Rigaud, "Bioelectrical impedance techniques in medicine," *Crit. Rev. Biomed. Eng.*, vol. 24, nos. 4–6, pp. 655–677, 1996.
- [2] K. Boone, D. Barber, and B. Brown, "Imaging with electricity: Report of the European concerted action on impedance tomography," *J. Med. Eng. Tech.*, vol. 21, no. 6, pp. 201–232, 1997.
- [3] A. A. Kaufman and G. V. Keller, *Induction Logging*. Amsterdam, The Netherlands: Elsevier, 1989.
- [4] J. R. Wait, *Geo-Electromagnetism*. New York: Academic, 1982.
- [5] P. P. Tarjan and R. McFee, "Electrodeless measurements of the effective resistivity of the human torso and head by magnetic induction," *IEEE Trans. Biomed. Eng.*, vol. BME-15, Oct. 1968.
- [6] P. P. Tarjan, "Electrodeless measurements of resistivity fluctuations in the human torso and head," Ph.D. dissertation, Syracuse Univ., Syracuse, NY, 1968.
- [7] D. C. Barber and B. H. Barber, "Applied potential tomography," *J. Phys. E: Sci. Instrum.*, vol. 17, pp. 723–733, 1984.
- [8] D. Isaacson, "Distinguishability of conductivities by electric current computed tomography," *IEEE Trans. Med. Imag.*, vol. 5, pp. 91–95, June 1986.
- [9] Y. Z. Ider, N. G. Gencer, E. Atalar, and H. Tosun, "Electrical impedance tomography of translationally uniform cylindrical objects with general cross sectional boundaries," *IEEE Trans. Med. Imag.*, vol. 37, pp. 624–631, Mar. 1990.
- [10] B. H. Brown and D. C. Barber, "Electrical impedance tomography," *Clin. Phys. Physiol. Meas.*, vol. 13, supp. A, p. 207, 1992.
- [11] W. R. Purvis, R. C. Tozer, and I. L. Freeston, "Induced current impedance imaging," *Proc. IEEE*, vol. 140, pt. A, pp. 135–141, Mar. 1993.
- [12] I. L. Freeston and R. C. Tozer, "Impedance imaging using induced currents," *Physiol. Meas.*, vol. 16, supp. 3A, pp. 257–266, 1995.
- [13] N. G. Gencer, "Electrical impedance tomography using induced currents," Ph.D. dissertation, METU, Ankara, Turkey, 1993.
- [14] N. G. Gencer, M. Kuzuoglu, and Y. Z. Ider, "Electrical impedance tomography using induced currents," *IEEE Trans. Med. Imag.*, vol. 30, June 1994.
- [15] N. G. Gencer, Y. Z. Ider, and S. J. Williamson, "Electrical impedance tomography: Induced current imaging achieved with a multiple coil system," *IEEE Trans. Med. Imag.*, vol. 43, pp. 139–149, Feb. 1996.
- [16] M. N. Tek and N. G. Gencer, "A new 3D FEM formulation for the solution of potential fields in magnetic induction problems," in *Proc. IEEE EMBS 19th Ann. Int. Conf.*, 1997.
- [17] N. G. Gencer and M. N. Tek, "Forward problem solution for electrical conductivity imaging via contactless imaging," *Phys. Med. Biol.*, vol. 44, no. 4, pp. 927–940, Apr. 1999.
- [18] B. D. Sollish, E. H. Frei, E. Hammerman, S. B. Lang, and M. Moshitzky, "Microprocessor-assisted screening techniques," *Isr. J. Med. Sci.*, vol. 17, pp. 859–864, 1981.
- [19] G. Piperno, E. H. Frei, and M. Moshitzky, "Breast cancer screening by impedance measurements," *Frontiers Med. Biol. Eng.*, vol. 2, no. 2, pp. 111–117, 1990.
- [20] N. D. Harris, A. J. Suggett, D. C. Barber, and B. H. Brown, "Applications of applied potential tomography (APT) in respiratory medicine," *Clin. Phys. Physiol. Meas.*, vol. 8, supp. A, pp. 155–165, 1987.
- [21] L. A. W. Smulders and A. van Oosterom, "Application of electrical impedance tomography to the determination of the lung volume," *Clin. Phys. Physiol. Meas.*, vol. 13, supp. A, pp. 167–170, 1992.
- [22] B. M. Eyuboglu, B. H. Brown, D. C. Barber, and A. D. Seagar, "Localization of cardiac related changes in the thorax," *Clin. Phys. Physiol. Meas.*, vol. 8, supp. A, pp. 167–173, 1987.
- [23] Y. F. Mangnall, A. J. Baxter, R. Avill, N. C. Bird, B. H. Brown, D. C. Barber, A. D. Seagar, A. G. Johnson, and N. W. Read, "Applied potential tomography: A new noninvasive technique for assessing gastric function," *Clin. Phys. Physiol. Meas.*, vol. 8, supp. A, pp. 119–129, 1987.
- [24] F. J. McArdle and B. H. Brown, "Imaging resistivity changes of the adult head during cardiac cycle," in *Proc. IEEE EMBS, 11th Ann. Int. Conf.*, 1989, p. 480.
- [25] F. J. McArdle, "Investigation of cardiosynchronous images of the heart and head using applied potential tomography," Ph.D. dissertation, Univ. Sheffield, Sheffield, U.K., 1992.
- [26] J. Conway, "Electrical impedance tomography for thermal monitoring of hyperthermia treatment: An assessment using *in vitro* and *in vivo* measurements," *Clin. Phys. Physiol. Meas.*, vol. 8, supp. A, pp. 141–146, 1987.
- [27] R. W. M. Smith, B. H. Brown, I. L. Freeston, and F. J. McArdle, "Real time electrical impedance tomography," in *Proc. CAIT Meeting Electrical Impedance Tomography*, Copenhagen, Denmark, 1990, pp. 212–216.
- [28] D. S. Holder, "Detection of cortical spreading depression in the anesthetized rat by impedance measurements with scalp electrodes. Implications for noninvasive imaging of brain with electrical impedance tomography," *Clin. Phys. Physiol. Meas.*, vol. 13, pp. 77–86, 1992.
- [29] K. G. Boone, A. M. Lewis, and D. S. Holder, "Imaging of cortical spreading depression using EIT: Implication of localization of epileptic foci," *Physiol. Meas.*, vol. 15, supp. 2A, pp. A189–A198, 1994.
- [30] M. S. Hamalainen and J. Sarvas, "Realistic conductivity geometry model of the human head for interpretation of neuromagnetic data," *IEEE Trans. Biomed. Eng.*, vol. 36, Feb. 1989.
- [31] Y. Yan, P. L. Nunez, and R. T. Hart, "Finite-element model of the human head: Scalp potentials due to dipole sources," *IFBME Med. Biol. Eng. Comput.*, vol. 29, pp. 475–481, 1991.
- [32] B. N. Cuffin, "EEG localization accuracy improvements using realistically shaped head models," *IEEE Trans. Biomed. Eng.*, vol. 43, Mar. 1996.
- [33] N. G. Gencer and M. N. Tek, "Imaging tissue conductivity via contactless measurements: A feasibility study," (in English) *TUBITAK Elektrik J.*, vol. 6, no. 3, 1998.
- [34] A. Ghahary, *Electrical Impedance Tomography*, J. G. Webster, Ed. Bristol, U.K.: IOP, 1990.
- [35] R. Plonsey and R. Collin, *Principles and Applications of Electromagnetic Fields*. New York: McGraw-Hill, 1961.
- [36] J. H. Tripp, "Physical concepts and mathematical models," in *Biomagnetism an Interdisciplinary Approach*, S. J. Williamson, G. L. Romani, L. Kaufman, and I. Modena, Eds. New York: Plenum, 1983, pp. 101–139.
- [37] W. H. Press, S. A. Teukolsky, W. T. Vetterling, and B. P. Flannery, *Numerical Recipes in C*. Cambridge, U.K., Cambridge Univ. Press, 1995, ch. 2, pp. 71–90.
- [38] G. H. Golub and C. F. Van Loan, *Matrix Computations*, 2nd ed. Baltimore, MD: Johns Hopkins Univ. Press, 1989.
- [39] E. H. Moore, "On the reciprocal of the general algebraic matrix," *Bull. Amer. Math. Soc.*, vol. 26, pp. 394–395, 1920.
- [40] R. Penrose, "A generalized inverse for matrices," in *Proc. Cambridge Philos. Soc.*, 1955, vol. 51, pp. 406–413.
- [41] Y. S. Shim and Z. H. Cho, "SVD pseudo-inversion image reconstruction," *IEEE Trans. Acoust. Speech, Signal Processing*, vol. ASSP-29, pp. 904–909, Aug. 1981.
- [42] B. J. Sullivan and B. Liu, "On the use of singular value decomposition and decimation in discrete-time band-limited signal extrapolation," *IEEE Trans. Acoust. Speech, Signal Processing*, vol. ASSP-32, Dec. 1984.
- [43] B. Jeffs, R. Leahy, and M. Singh, "An evaluation of methods for neuromagnetic image reconstruction," *IEEE Trans. Med. Imag.*, vol. BME-34, pp. 713–723, Sept. 1987.
- [44] N. G. Gencer and S. J. Williamson, "Differential characterization of neural sources with the bimodal truncated SVD pseudo-inverse for EEG and MEG measurements," *IEEE Trans. Biomed. Eng.*, vol. 45, pp. 827–838, July 1998.